On the Role of Wind–Evaporation–SST Feedbacks in the Subseasonal Variability of the East Pacific ITCZ

INDRANI GANGULY,[a] ALEX O. GONZALEZ,[a,b] AND KRISTOPHER B. KARNAUSKAS[c,d]

[a] *Department of Geological and Atmospheric Sciences, Iowa State University, Ames, Iowa*
[b] *Department of Physical Oceanography, Woods Hole Oceanographic Institution, Woods Hole, Massachusetts*
[c] *Department of Atmospheric and Oceanic Sciences, University of Colorado Boulder, Boulder, Colorado*
[d] *Cooperative Institute for Research in Environmental Sciences, University of Colorado Boulder, Boulder, Colorado*

(Manuscript received 17 November 2022, in final form 19 September 2023, accepted 13 October 2023)

ABSTRACT: The intertropical convergence zone (ITCZ) is a zonally elongated band of near-surface convergence and precipitation near the equator. During boreal spring, the eastern Pacific ITCZ migrates latitudinally on daily to subseasonal time scales, and climate models exhibit the greatest ITCZ biases during this time of the year. In this work, we investigate the air–sea interactions associated with the variability in the eastern Pacific ITCZ's latitudinal location for consecutive days when the ITCZ is only located north of the equator (nITCZ events) compared to when the ITCZ is on both sides of the equator or south of the equator (dsITCZ events) during February–April. The distribution of sea surface temperature (SST) anomalies and surface latent heat flux (SLHF) anomalies during the nITCZ and dsITCZ events follow the classic wind–evaporation–SST (WES) positive feedback mechanism. However, an alternative mechanism, embracing the effect of SST anomalies on vertical stratification and momentum mixing, gives rise to a negative WES feedback. Our results show that in the surface layer, there is a general progression of positive WES feedbacks happening in the weeks leading to the events followed by negative WES feedbacks occurring after the ITCZ events, with an alternate mechanism involving air–sea humidity differences limiting evaporation occurring in between. Additionally, the spatial structures of the components of the feedbacks are nearly mirror images for these opposite ITCZ events over the east Pacific during boreal spring. In closing, we find that understanding the air–sea interactions during daily to weekly varying ITCZ events (nITCZ and dsITCZ) helps to pinpoint how fundamental processes differ for ITCZs in different hemispheres.

KEYWORDS: Intertropical convergence zone; Atmosphere-ocean interaction; Air-sea interaction; Subseasonal variability

1. Introduction

The intertropical convergence zone (ITCZ) can be described as a zonally elongated band of near-surface wind convergence in the equatorial trough, typically collocated with heavy precipitation. Unlike over the continental landmasses, where the ITCZ follows the seasonal insolation at a 1-month delay (Waliser and Gautier 1993), the latitudinal migration of the ITCZ over the oceans is less pronounced and depends on numerous other factors, such as air–sea interactions, continental geometry, and cloud-radiative effects (e.g., Philander et al. 1996; Li and Philander 1996; Voigt et al. 2014; Adam et al. 2016b). Recent studies have shown that the ITCZ position varies on smaller time scales of days to weeks over the east Pacific Ocean (Henke et al. 2012; Haffke et al. 2016; Gonzalez et al. 2022). The ITCZ can even shift hemispheres during February through April, for example, alternating between an ITCZ in the Southern Hemisphere, Northern Hemisphere, or a double ITCZ (one ITCZ in each hemisphere simultaneously) multiple times within a season (Haffke et al. 2016; Gonzalez et al. 2022; Yang and Magnusdottir 2016). Improving our understanding of these submonthly shifts in the east Pacific ITCZ's position could be important in highlighting key mechanisms that drive ITCZs in each hemisphere. This is especially true considering the overarching problem in climate models in their inability to replicate the position of the ITCZ (Mechoso et al. 1995; Lin 2007; Bellucci et al. 2010; Zhang et al. 2015; Oueslati and Bellon 2015; Fiedler et al. 2020). This is often called "the double ITCZ problem" because of one annual tropical precipitation maximum being present in each hemisphere rather than just north of the equator.

The double ITCZ problem is particularly prevalent during January through May over the east Pacific Ocean and the Atlantic Ocean (Adam et al. 2018; Song and Zhang 2019; Tian and Dong 2020; Si et al. 2021), and the precipitation bias is exacerbated in atmosphere–ocean coupled models (Xiang et al. 2017) due in part to wind–evaporation–sea surface temperature (SST) feedbacks (Xie and Philander 1994; Lin 2007; Zhang et al. 2019) and Bjerknes feedbacks (Bjerknes et al. 1969; Zhang 2001; Lin 2007; Li and Xie 2014). Furthermore, both wind–evaporation–SST (WES) feedbacks and Bjerknes feedbacks can be more broadly linked to interhemispheric temperature and energy asymmetries (Broccoli et al. 2006; Kang et al. 2008; Chiang and Friedman 2012; Frierson and Hwang

---

Denotes content that is immediately available upon publication as open access.

Supplemental information related to this paper is available at the Journals Online website: https://doi.org/10.1175/JCLI-D-22-0849.s1.

Corresponding author: Indrani Ganguly, iganguly@iastate.edu

DOI: 10.1175/JCLI-D-22-0849.1

2012) and/or anomalously weak atmospheric net energy input (e.g., Bischoff and Schneider 2014, 2016; Adam et al. 2016a; Schneider 2017; Adam et al. 2018). Interhemispheric energy asymmetries can arise due to the influence of remote forcings, such as high-latitude ice-cover changes (Chiang and Bitz 2005; Hwang and Frierson 2013), or forcings with tropical origins (Xiang et al. 2017; Adam et al. 2018; Xiang et al. 2018) as well as asymmetric radiative forcings from volcanic eruptions (Pausata et al. 2015; Colose et al. 2016; Yang et al. 2019).

Karnauskas (2022) used an idealized air–sea coupled model to show the effects of WES feedbacks following two mechanisms, one anchored by Lindzen and Nigam (1987, mechanism LN87) as proposed by Xie and Philander (1994) and the other anchored by Hayes et al. (1989) and Wallace et al. (1989, mechanism WH89). The LN87 mechanism drives a positive feedback between near-equatorial north–south SST gradients, north–south surface pressure gradients, near-surface winds, and latent heat fluxes, which together cause the initial SST gradient to intensify with time. On the other hand, the WH89 drives a negative feedback mechanism involving the north–south SST gradients, vertical stratification, and vertical momentum mixing, causing the SST gradient to weaken with time. The simple model developed by Karnauskas (2022) allows for both the mechanisms to exist simultaneously and showed that under idealized conditions near the equator, the evolution of the model follows LN87 for a few months, after which the WH89 acts to dampen the positive feedback on longer time scales. While WES feedbacks have been seen in models and observations for seasonal or longer time scales (Hayes et al. 1989; Wallace et al. 1989; Xie and Philander 1994; Chelton et al. 2001; Li and Xie 2014), it is less clear if these mechanisms occur during submonthly ITCZ shifting and splitting events (Gonzalez et al. 2022).

In this study, we quantify whether the “fingerprints” of positive LN87 and negative WH89 WES mechanisms coexist in the weeks prior to and following February–April subseasonal ITCZ events over the east Pacific Ocean using reanalysis data. We also determine whether the atmosphere–ocean variables that drive the WES feedbacks are structurally antisymmetric during Northern Hemisphere versus Southern Hemisphere ITCZ events.

The paper is organized as follows: Section 2 describes the observational and reanalysis datasets used as well as the submonthly ITCZ events dataset created from three-hourly ITCZ states (Haffke et al. 2016; Gonzalez et al. 2022). We also present the methods used to calculate saturation specific humidity, the method used to compute the climatology and anomalies of all fields, and we discuss the fundamental ideas of positive and negative WES feedback mechanisms. Section 3 has four subsections, with the first motivating the investigation by showing the total precipitation and wind patterns and their anomalies for the two ITCZ states being studied. In the next two subsections of section 3, we illustrate the positive and negative WES feedback mechanisms through time evolution of composites of the surface latent heat flux (SLHF) and the behavior of SSTs for ITCZ events, as well as the near-surface zonal and meridional wind anomalies and air temperature. The last subsection of section 3 discusses the time evolution of the two feedback mechanisms. Section 4 summarizes our results and discusses future directions to better understand February–April east Pacific ITCZ events.

2. Data and methods

a. Observational and reanalysis data

Daily precipitation rates are obtained from the Tropical Rainfall Measuring Mission (TRMM) Multisatellite Precipitation Analysis (TMPA) dataset for 1998–2012, February–April, at a 0.25° resolution (Huffman and Bolvin 2015). Daily averaged SSTs, 10- and 100-m horizontal winds, 10-m air temperature, mean sea level pressure, SLHF, and specific humidity of air are calculated from six-hourly output from the European Centre for Medium-Range Weather Forecasts (ECMWF) ERA5 reanalysis for 1980–2012, February–April, at 0.25° resolution (Hersbach et al. 2020). Anomalies for all variables are computed by removing a climatological annual cycle that is smoothed using the first three harmonics of the raw annual cycle. Additionally, the linear least squares trend and time mean are removed for all anomalies, and all variables have a land–sea mask applied to focus solely on variability over the ocean.

For the computation of individual terms within the ERA5 SLHF bulk aerodynamic formula, saturation specific humidity is required. Saturation specific humidity is computed from ERA5 saturation water vapor pressure $e_{\text{sat}}(T)$, obtained from Tetens’ formula (Tetens 1930; ECMWF 2016), and mean sea level pressure p via the formula

$$Q_s = \frac{\dfrac{R_{\text{dry}}}{R_{\text{vap}}} e_{\text{sat}}(T)}{p - \left(1 - \dfrac{R_{\text{dry}}}{R_{\text{vap}}}\right) e_{\text{sat}}(T)}, \tag{1}$$

where T is the SST and R_{dry} and R_{vap} are the dry air and water vapor gas constants, respectively.

At the heart of WES feedbacks is the relationship between SST tendencies that correspond to the SLHF via the formula

$$\frac{\partial T}{\partial t} = -\frac{\text{SLHF}}{\rho C_p h}, \tag{2}$$

where $\rho = 1025$ kg m^{-3}, $C_p = 3850$ J kg^{-1} K^{-1}, and h is the mixed layer depth. We refer to this formula throughout the paper and use ERA5 SLHF and h from the Global Ocean Reanalysis and Simulation (GLORYS-12v1; Lellouche et al. 2018; Jean-Michel et al. 2021) at a 1/12° resolution to estimate SST tendencies resulting solely from SLHF anomalies.

b. Submonthly ITCZ events dataset

Henke et al. (2012) devised a pattern recognition algorithm that quantified the spatial extent and temporal variability of the ITCZ using 5 years (2000–04) of GridSat satellite data (Knapp et al. 2011) over 20°S–20°N and 90°W–180°. Four ITCZ states were determined: north ITCZ (nITCZ), when the ITCZ lies only to the north of the equator; south ITCZ (sITCZ), when the ITCZ lies only to the south of the equator; double ITCZ (dsITCZ), when one ITCZ straddles the equator in each hemisphere; and absent ITCZ (aITCZ), when no zonally elongated convergence band is seen. A fifth state called equatorial ITCZ

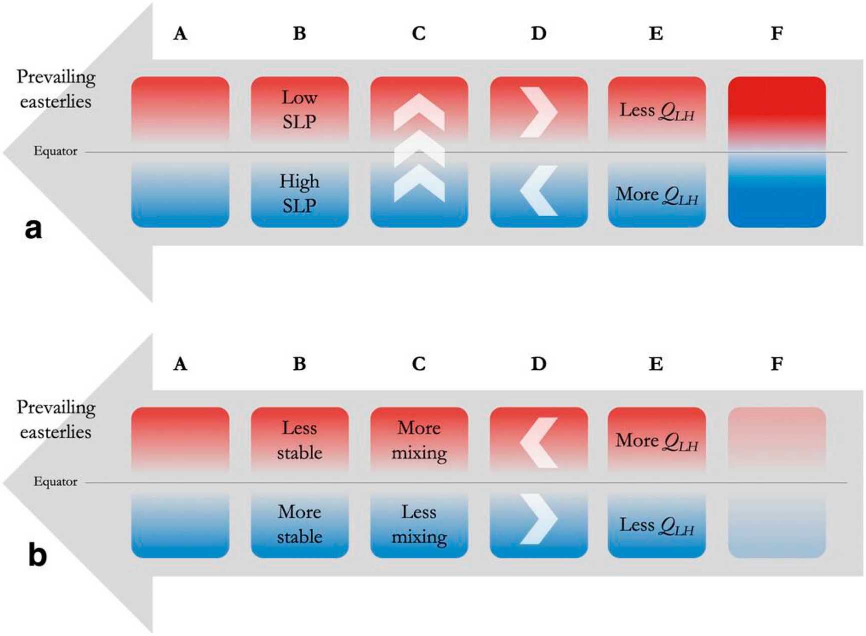

FIG. 1. (a) Schematic of the positive WES feedback mechanism (LN87), following hydrostatic balance. Warm SSTs get warmer and cold SSTs get colder. (b) Schematic of the negative WES feedback mechanism (WH89), following vertical momentum mixing. Warmer SSTs become less warm and colder SSTs become less cold. [Reproduced from Karnauskas (2022) with permission from AMS.]

(eITCZ) was added in Haffke et al. (2016) when the ITCZ lies over the equator. Haffke et al. (2016) also extended the Henke et al. (2012) pattern recognition algorithm to 33 years (1980–2012) of 3-hourly GridSat infrared imagery, producing a dataset used in Gonzalez et al. (2022) to create submonthly ITCZ events for February–April 1980–2012. Submonthly ITCZ events are comprised of daily ITCZ states that last for 2–30 consecutive days. The distribution of the submonthly ITCZ events shows that nITCZ events occur the most (44.9%), followed by dsITCZ events (27.6%), aITCZ events (14.7%), eITCZ events (7.2%), and sITCZ events (5.6%), which is shown along with temporal distribution in Fig. S1 in the online supplemental material. Since the pattern of the anomalies associated with dsITCZ and sITCZ events is highly correlated (e.g., Yang and Magnusdottir 2016, and Fig. S2) and in order to increase the sample size of events when a southern ITCZ is present, dsITCZ and sITCZ events are grouped together (occurring 33.2% of the time); they will be referred to as dsITCZ events from here on. Essentially, these dsITCZ events represent when there exists an ITCZ south of the equator. Since nITCZ events occur most frequently followed by dsITCZ events and climate models tend to overproduce double and southern ITCZs during February–April (e.g., Adam et al. 2018; Si et al. 2021), we focus on these two events for this study.

In composite mean analyses, we shift the time dimension back by 31 days (lag = −31) and forward by 31 days (lag = 31) to show the time-lag evolution over 62 days of each field surrounding nITCZ and dsITCZ events.

c. *Positive and negative wind–evaporation–SST feedbacks*

Since the effect of both positive and negative WES feedbacks on northern and double-southern ITCZs is a central component of this study, we describe the basic underlying concepts of the two mechanisms below.

As shown in Fig. 1a, the positive WES feedback for a northern ITCZ begins with anomalously cool and warm SSTs south and north of the equator, respectively (column A). This anomalous northward SST gradient is associated through hydrostatic balance with an anomalous northward surface pressure gradient force (column B) that enhances the southerly flow across the equator (column C). This southerly anomaly is deflected by the Coriolis force resulting in anomalous easterlies and westerlies south and north of the equator, respectively (column D). Since the background flow is easterly, there are higher wind speeds south of the equator and lower wind speeds north of the equator, which results in more evaporation/ocean cooling south of the equator and vice versa north of the equator (columns E and F). This enhances the northward SST gradient and brings us back to the beginning of the positive feedback loop (column A).

As shown in Fig. 1b, the negative WES feedback for a northern ITCZ begins just like the positive WES feedback (column A), but it considers the effect of the temperature stratification on changes to surface winds. Assuming the temperature profile is unchanged above the surface, the lower troposphere is more statically stable (cool below

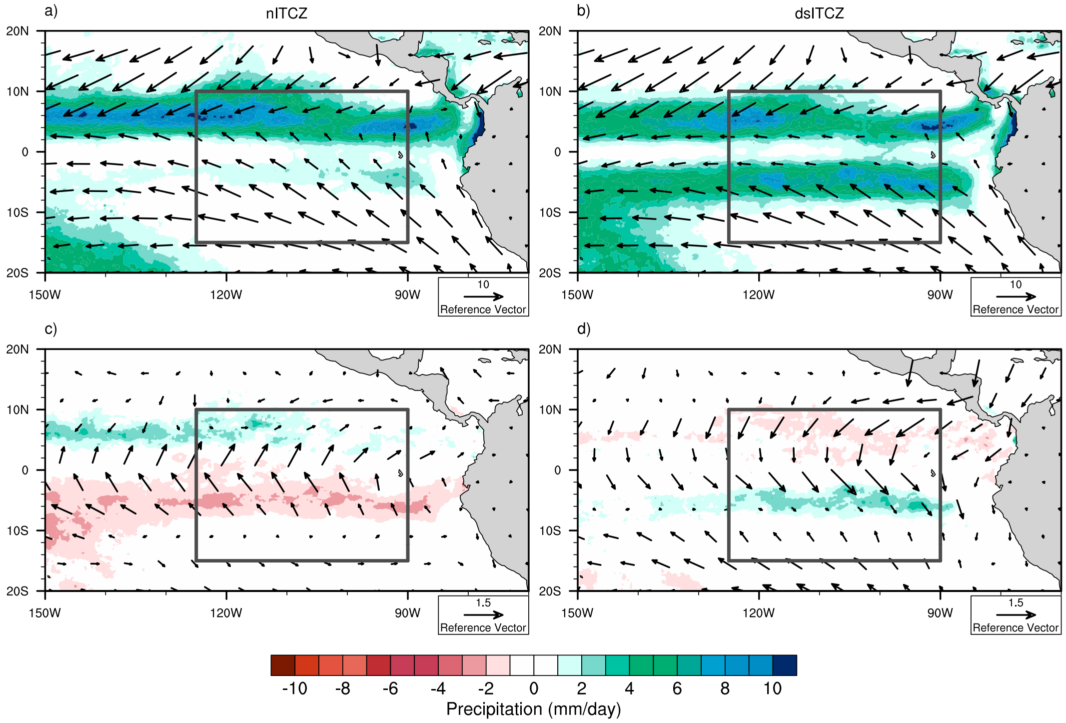

FIG. 2. Mean precipitation obtained from TRMM-TMPA (shaded) and mean surface winds obtained from ECMWF ERA5 (vectors), averaged over February–April 1980–2012, for (a) nITCZ and (b) dsITCZ events. Corresponding anomalies in precipitation and surface winds for (c) nITCZ and (d) dsITCZ events.

warm) and turbulent mixing decreases south of the equator, and vice versa north of the equator (column B). Assuming that there is stronger easterly flow above, there is a decrease in momentum mixing south of the equator, and vice versa for north of the equator (column C). Thus, momentum mixing produces anomalous westerlies and easterlies south and north of the equator, respectively (column D). These anomalies are opposite as those in the positive WES feedback mechanism, and so, there is less evaporation/ocean cooling south of the equator and vice versa north of the equator (columns E and F). Since the initial northward SST gradient becomes weaker with time, momentum mixing due to changes in vertical stratification is considered a negative WES feedback mechanism.

To guide this study, we follow the fingerprints of opposing flavors of WES mechanisms outlined above. Since both the feedback mechanisms start off with the same gradient of SSTs, to confirm the presence of each WES feedback, we analyze the variables associated with columns B–E and we hypothesize whether column F occurs. For the positive WES feedback mechanism, we analyze the spatial structures of anomalous mean sea level pressure (MSLP), meridional and zonal surface winds, and SLHF. For the negative WES feedback mechanism, we analyze the spatial structures of near-surface temperature stratification, zonal and meridional wind shear, and SLHF. However, since column E has opposing SLHF anomalies for the two WES feedback mechanisms, we only "see" the SLHF anomalies of the dominant WES feedback mechanism. We also look at the time evolution of SSTs from 4 weeks before the ITCZ event to 4 weeks after to hypothesize the order of occurrence of the two opposing feedback mechanisms.

3. Results

a. *Composites of precipitation and surface winds during nITCZ and dsITCZ events*

From Fig. 2b, it is evident that during dsITCZ events, there are strong bands of zonally elongated precipitation south and north of the equator, both at 2°–8°. Contrasting this with the nITCZ events (Fig. 2c), this precipitation is anomalously positive south of the equator and anomalously negative north of the equator (Fig. 2d). It is also notable that the wind speeds decrease considerably and the winds converge at the latitudes where the precipitation maximizes (the ITCZ) in Figs. 2a,b. In Figs. 2c,d, strong anomalous cross-equatorial flow into the northern and southern ITCZ is present, which changes from southeasterly to southwesterly in the case of nITCZ events and from northeasterly to northwesterly in the case of dsITCZ events. The black rectangle in Fig. 2 marks the region of interest for this study and ranges from 90° to 125°W and from 10°N to 15°S. This region enables us to represent the significant anomalous dynamical and thermodynamic features associated with both nITCZ and dsITCZ events, without taking into consideration the effects of South Pacific convergence zone (SPCZ).

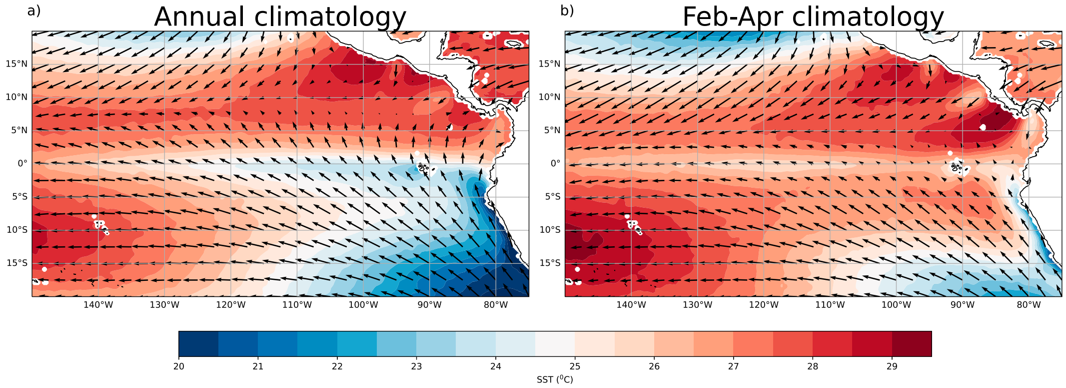

FIG. 3. Mean SST in (a) annual climatology and (b) February–April climatology over the east Pacific.

b. *Positive WES feedback: Hydrostatic adjustment of sea level pressure*

This section is divided into three subsections. The first two subsections reveal the time evolution and spatial structures associated with individual steps in the positive WES feedback mechanism in reanalysis data, looking at the near-surface SST gradients and dynamics, respectively. The third subsection describes the connection of the dynamics and SSTs to surface latent heat fluxes associated with this mechanism.

1) SST ANOMALIES AND TIME EVOLUTION OF SST GRADIENT

In the annual mean, SSTs are higher north of the equator in what is commonly called the east Pacific warm pool and there is an equatorial cold tongue due to Ekman upwelling, shown in Fig. 3. This persistent climatological northward SST gradient and mean northward ITCZ position explains the dominance of the positive WES feedback over the negative WES feedback to first order.

Figures 4a and 4b show the distribution of zonally averaged (90°–125°W) anomalous SST at daily lags of 21 days before to 21 days after nITCZ and dsITCZ events. Because we classify ITCZ events as ITCZ states persisting for 2–30 days, 42 days encompassing an ITCZ event is a reasonable time frame to study the signature of the WES feedback mechanisms. For nITCZ events, there exists an anomalously positive SST gradient to the north of the equator due to the anomalous strong cold tongue present at 0°–2°S and the warmest SSTs at 10°N. For dsITCZ events, SSTs are anomalously positive in two limited regions south of the equator, 2°–5°S and south of 12°S. In contrast to nITCZ events, anomalously cold SSTs are present near the ITCZ latitudes (Fig. 2), over 5°–11°S, for dITCZ events. This region is also characterized by anomalously warm boundary layer air (not shown). Despite this unexpected cold SST feature, there is a strong southward SST gradient from 2°S to 2°N for dsITCZ events, which is associated with a strong cold SST anomaly north of the equator. For both ITCZ events, the latitudinal location of the anomalously positive SSTs coincides with the latitudinal extent of the anomalously positive precipitation (Fig. 2), with the exception of 5°–11°S for dsITCZ events. To broadly quantify the time evolution of positive and negative WES feedbacks, we select two regions, one around the warmest statistically significant SST anomalies (red shaded) and one around the coldest statistically significant SST anomalies (blue shaded) for both types of ITCZ events. The difference in SST anomalies in these two regions represents the anomalous SST gradient per degree latitude, shown in Figs. 4c and 4d as a function of time, from 31 days before to 31 days after each ITCZ event.

For nITCZ events, there is a general increase in the SST gradient leading up to the day of the event (lag 0) and a decrease in the SST gradient after the event. This suggests the positive WES feedback is active in the days or weeks before an nITCZ occurs and the negative WES feedback takes over after the event. For dsITCZ events, the increase in SST gradient is seen up until 10 days before the event (positive WES feedback) after which the gradient decreases, which suggests the presence of the negative WES feedback mechanism.

2) MSLP, NEAR-SURFACE MERIDIONAL WIND, AND ZONAL WIND ANOMALIES

In Fig. 5a, 6°–8°N in red shading (P_N) refers to a region of relatively low MSLP anomalies (corresponding to the statistically significant highest SST anomalies in Fig. 4) and 2°S–0° in blue shading (P_S) refers to a region with relatively higher MSLP anomalies (corresponding to statistically significant anomalously low SSTs Fig. 4). There is a broad trend toward negative MSLP anomalies from lag −21 to lag 21 for nITCZ events and the cross-equatorial MSLP gradient ($P_N - P_S$) is strongest at lag −11 and generally weakens thereafter. A relative maximum in cross-equatorial MSLP gradient occurs 1 day before the ITCZ event (Fig. 5c) and rapidly weakens in the days following the event.

For dsITCZ events in Fig. 5b, 5°–7°S in red shading (P_S) indicates anomalously lower MSLP corresponding to higher SST anomalies in Fig. 4 and 4°–6°N in blue shading (P_N) is the region of anomalously high MSLP due to cold SST anomalies. The MSLP gradient, $P_S - P_N$, is generally constant in the days and weeks leading up to the event, with numerous oscillations. After the dsITCZ event, the cross-equatorial gradient decreases steadily with time.

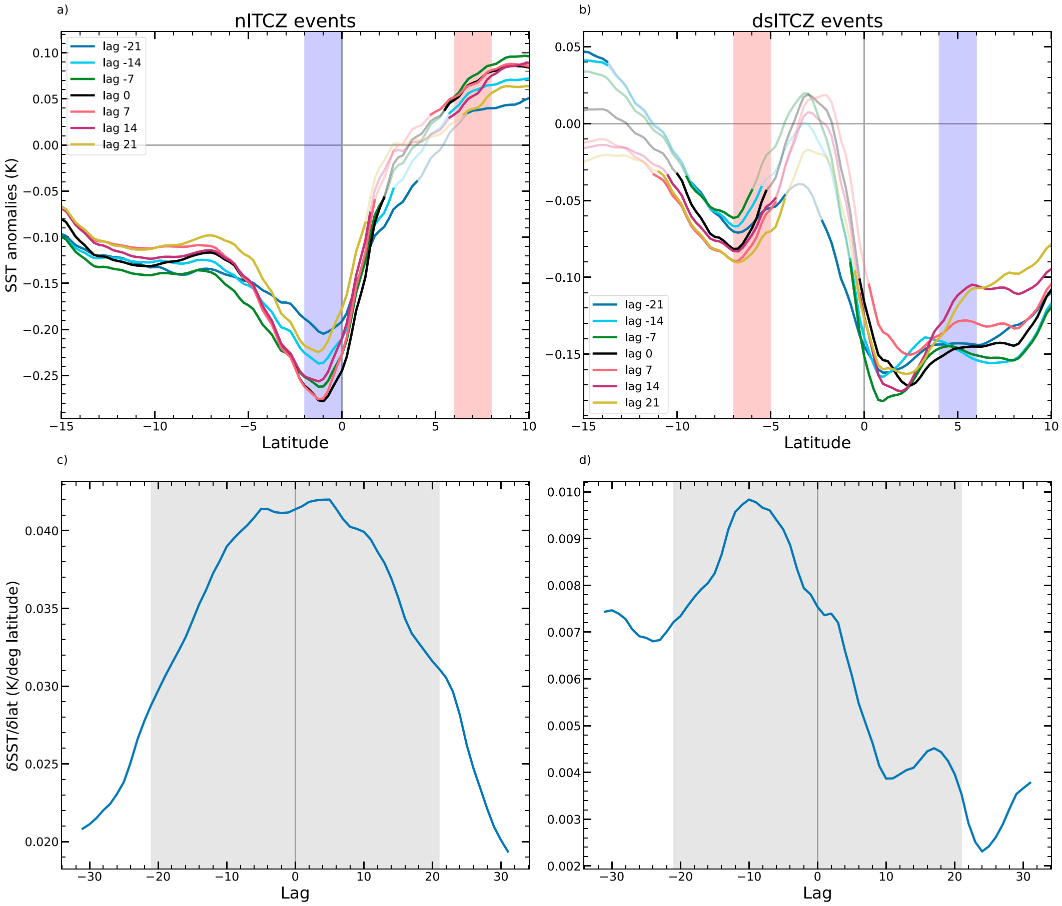

FIG. 4. Zonally averaged (90°–125°W) SST anomalies of (a) nITCZ events and (b) dsITCZ events from 21 days before to 21 days after each event. Opaque lines show SST at 95% confidence levels using a two-tailed *t* test. (c),(d) The time evolution of cross-equatorial SST gradient between the red region (6°–8°N for nITCZ; 5°–7°S for dsITCZ) and blue region (2°S–0° for nITCZ; 4°–6°N for dsITCZ) from 31 days before to 31 days after nITCZ and dsITCZ events.

The anomalously low MSLP to the north of the equator for nITCZ events in Fig. 5a sets up near-surface (10 m) southerly wind anomalies across the equator through the meridional pressure gradient force, shown in Fig. 5e. Furthermore, there are anomalously stronger southerlies corresponding to enhanced wind convergence at 2°–5°N. For dsITCZ events, strong anomalous cross-equatorial northerlies are present in Fig. 5f following the negative MSLP gradient to the south of the equator in Fig. 5b. The cross-equatorial winds are deflected due to the Coriolis effect, creating a zonal wind acceleration on top of the background climatological easterly winds (Fig. 3 vectors). For nITCZ events, this results in anomalous westerlies (weaker easterlies) to the north and stronger easterlies to the south of the equator during nITCZ events, as seen in Fig. 5g. During dsITCZ events, anomalous westerlies are produced south of the equator, peaking at the spatial location of anomalously positive precipitation. To the north of the equator, stronger easterlies are present (Fig. 5h). Thus, the composite mean nITCZ and dsITCZ anomalous meridional and zonal surface winds follow along qualitatively with columns C and D of Fig. 1a.

For both these ITCZ events, the MSLP gradient becomes strongest before lag 0 and generally weakens after lag 0. This timing is generally consistent with SST gradients, particularly after lag 0. Furthermore, both the zonal and meridional wind anomalies are largest at lag 0 (black lines in Figs. 5a–h), in agreement with Gonzalez et al. (2022). The time delay between the strongest SST/MSLP gradients and dynamical fields suggests that the positive WES feedback is a key ingredient to both nITCZ and dsITCZ events.

3) SLHF ANOMALIES AND POSITIVE WES FEEDBACK

The second to last step/process in the positive WES feedback incorporates how changes in wind speeds are associated with variations in SLHF (column E of Fig. 1a). According to the Northern Hemisphere ITCZ example of the positive WES feedback in Fig. 1a, anomalous southeasterly and southwesterly surface winds south and north of the equator result in an increase in SLHF to the south and a decrease in latent heat flux to the north of the equator. To diagnose this behavior, we decompose SLHF via the bulk aerodynamic formula in ERA5. In this formula,

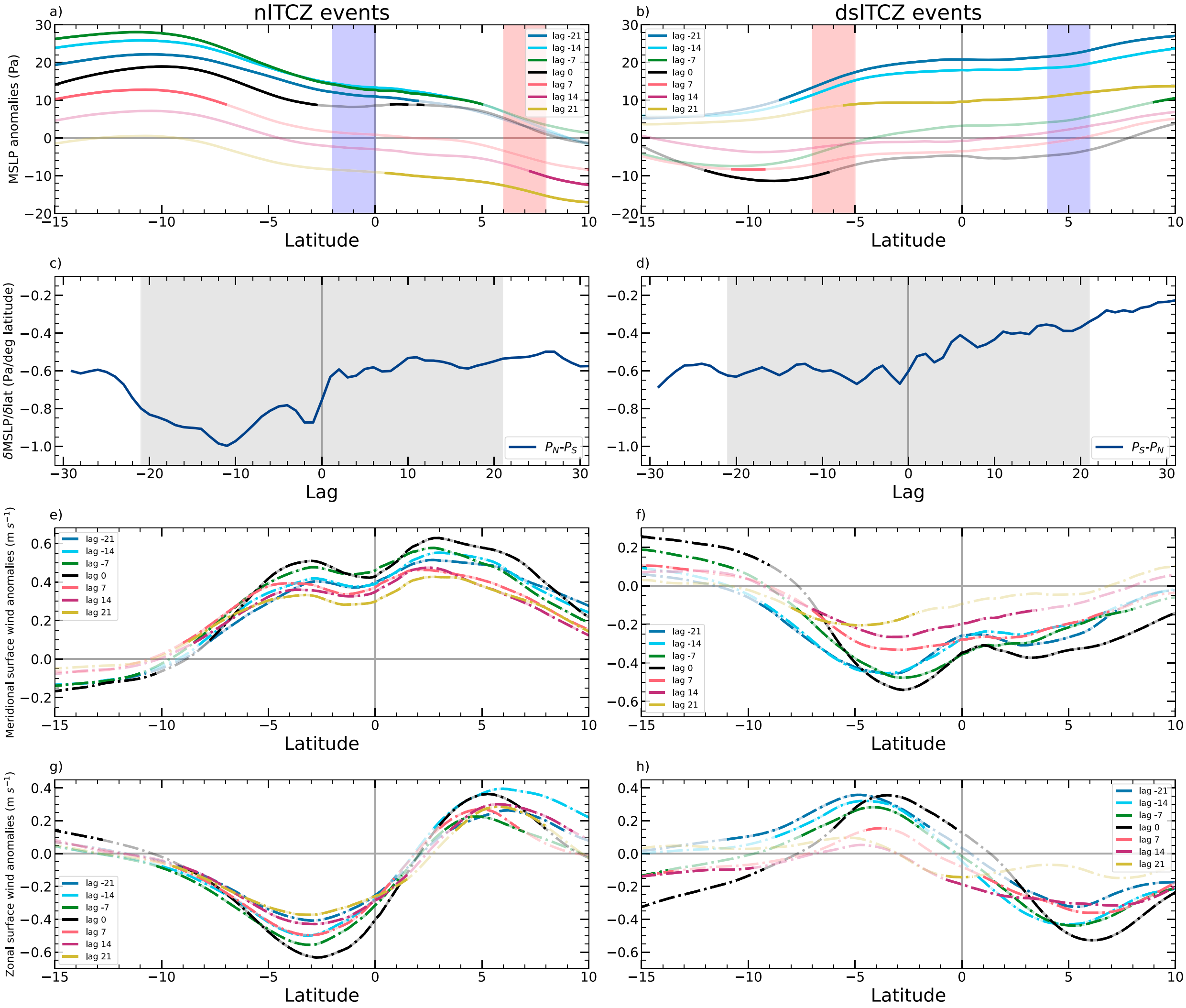

FIG. 5. Zonally averaged (90°–125°W) anomalies of (a),(b) MSLP, (e),(f) meridional surface wind, and (g),(h) zonal surface wind anomalies of (left) nITCZ and (right) dsITCZ events from 21 days before to 21 days after each event. The opaque lines show the fields at 95% confidence level using a two-tailed t test. (c),(d) Time evolution of cross-equatorial MSLP gradient between the red region (6°–8°N for nITCZ; 5°–7°S for dsITCZ) and blue region (2°S–0° for nITCZ; 4°–6°N for dsITCZ) from 31 days before to 31 days after nITCZ and dsITCZ events.

SLHF is a function of air density ρ, moisture exchange coefficient C_e, latent heat of vaporization L_v, surface saturation specific humidity Q_s, 10-m air specific humidity Q_a, and 10-m wind speed U_{10} given by

$$\text{SLHF} = \rho C_e L_v (Q_s - Q_a) U_{10}. \tag{3}$$

The climatological SLHF can be written as

$$\overline{\text{SLHF}} = \rho C_e L_v (\overline{Q_s} - \overline{Q_a}) \overline{U_{10}}, \tag{4}$$

where each term with an overbar is the climatological average. It is to be noted that the bulk formulas in Eqs. (3) and (4) neglect surface-to-surface air temperature differences, which in some cases might be important (Siler et al. 2019). Assuming $\rho C_e L_v$ to be constant, where $\rho = 1.2$ kg m^{-3}, $C_e = 1.1 \times 10^{-3}$ (Fairall et al. 2003), and $L_v = 2.5 \times 10^6$ J kg^{-1}, we can decompose the SLHF anomaly as

$$\delta\text{SLHF} = \rho C_e L_v \Big[\underbrace{(\overline{Q_s} - \overline{Q_a}) \delta U_{10}}_{\text{dynamic}} + \underbrace{\delta(Q_s - Q_a) \overline{U_{10}}}_{\text{thermodynamic}} + \underbrace{\delta(Q_s - Q_a) \delta U_{10}}_{\text{covariant}} \Big] + \text{residual}, \tag{5}$$

where each term with a $\delta(\cdot)$ is the anomaly. From Eq. (5), variations in SLHF can be driven to first order by anomalous 10-m wind speeds (dynamic component of SLHF), differences between the anomalous 10-m and saturation specific humidity (thermodynamic component of SLHF), or a combination of both (covariant component of SLHF). Since both positive and

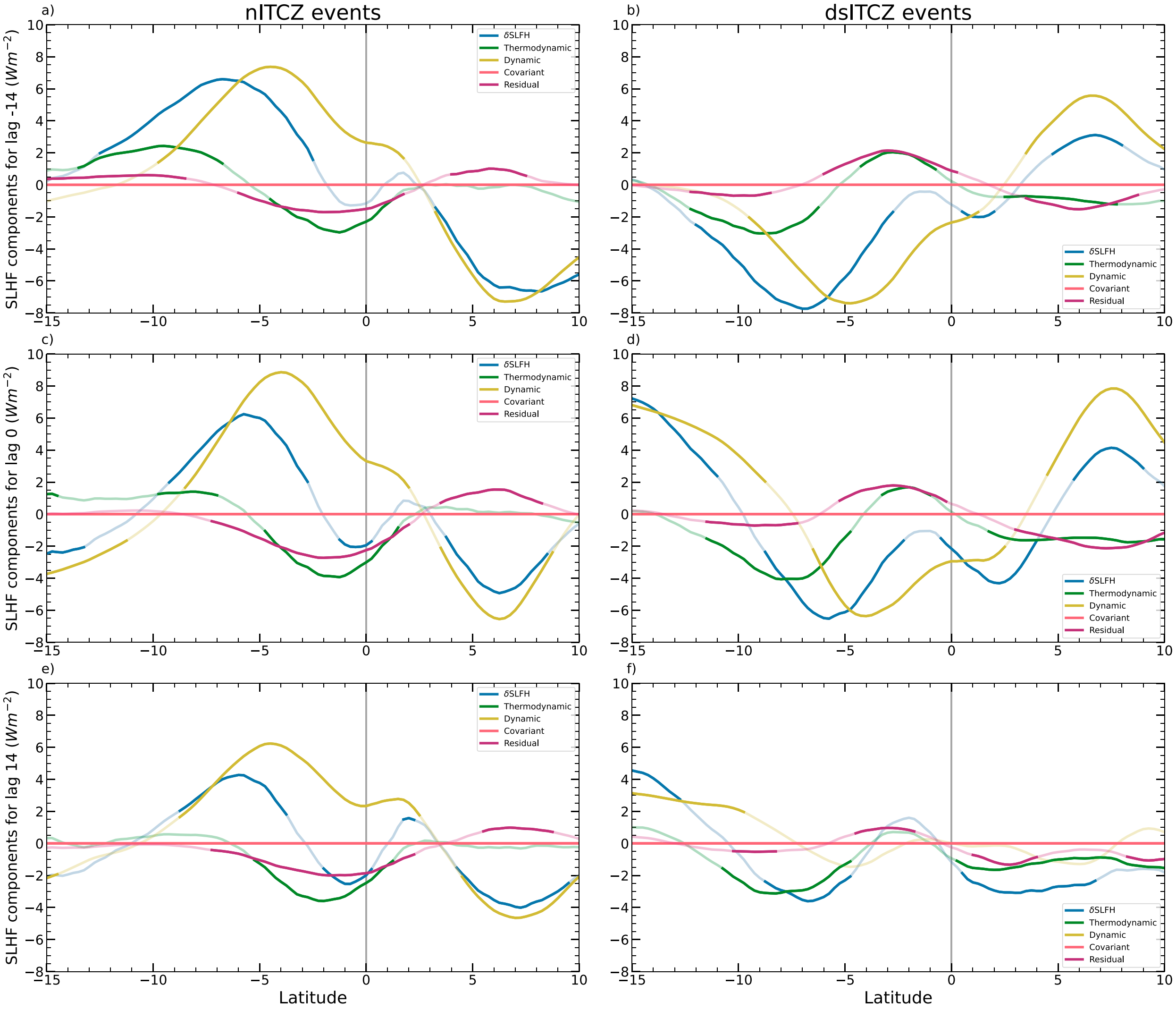

FIG. 6. Zonally averaged (90°–125°W) anomalies of SLHF for (left) nITCZ and (right) dsITCZ events. The anomalous SLHF (blue curves) along with its thermodynamic (green curves), dynamic (yellow curves), and covariant (pink curves) components, and residual (purple curves) are shown for (a),(b) 14 days before the event, (c),(d) day of the event, and (e),(f) 14 days after the event. Opaque lines show the fields at 95% confidence using a two-tailed *t* test.

negative WES feedbacks involve only the effects of changes in wind speeds on SLHF anomalies, they apply to the dynamic component of SLHF. At the same time, we expect the thermodynamic component to be important in damping positive WES feedbacks (Karnauskas 2022).

Figure 6 shows the anomalous SLHF along with its thermodynamic, dynamic, and covariant components, and the residual from Eq. (5) for nITCZ and dsITCZ events for 14 days before the event (Figs. 6a,b), day of the event (Figs. 6c,d), and 14 days after the event (Figs. 6e,f). From Figs. 4c and 4d, 10–20 days before and after lag 0 capture the strong increase and decrease in SST gradients quite well for both types of events. Looking at lag −14 and lag 14 provides a reasonable snapshot of the time evolution of SLHF following the SST tendency. Focusing first at lag −14 and the anomalous SLHF (blue curves), nITCZ events are characterized by a strong positive SLHF anomaly south of the equator (2°–10°S), where anomalously strong wind speeds and weak precipitation exist (Figs. 2a,b). In addition, there is a strong negative SLHF anomaly north of the equator (3°–10°N), where winds are anomalously weak and the ITCZ precipitation band exists (Figs. 2a,b). The amplitude of SLHF is quite similar between lag −14 and 0 and weakens by lag 14, particularly at the off-equatorial peaks.

For dsITCZ events (right panels of Fig. 6), the anomalous SLHF (blue curves) structure is similar to nITCZ events but with the opposite sign. Strong negative SLHF anomalies are observed at 5°–7°S, coinciding with weaker wind speeds and the location of the anomalous ITCZ precipitation to the south of the equator (Figs. 2c,d). SLHF anomalies are positive north of 3°N where wind speeds are larger and negative precipitation anomalies peak (Figs. 2c,d). While the negative SLHF region south of the equator generally weakens from lag −14 to 0 and to 14, the positive SLHF region north of the equator strengthens from lag −14 to 0 and weakens substantially by lag 14.

Considering there is a broad anticorrelation between SLHF and horizontal wind speeds for nITCZ and dsITCZ events, it is not surprising that the dynamic SLHF component (yellow curves) is structurally more similar to the anomalous SLHF (blue curves) off the equator. At the same time, the anomalous SLHF is shifted 1°–2° southward of the dynamic SLHF in the Southern Hemisphere due to the relatively strong constructive interference of the thermodynamic SLHF component (green curves). The thermodynamic SLHF becomes even more important near the equator because the dynamic SLHF is smaller. In fact, the thermodynamic SLHF helps explain why the anomalous SLHF often changes signs near the equator for both nITCZ and dsITCZ events. However, the residual is of a comparable magnitude to the thermodynamic component near the equator for dsITCZ events, so some caution must be taken. The covariant SLHF is generally small enough compared to the dynamic, thermodynamic, and residual terms during both nITCZ and dsITCZ events and is thus considered unimportant in this analysis.

To first order in nITCZ and dsITCZ events, SLHF anomalies are dominated by the dynamic SLHF component, that is, where wind speeds are anomalously strong, SLHF are anomalously large and vice versa for anomalously weak wind speeds (column E of Fig. 1a). However, the dynamic SLHF component weakens and the thermodynamic component strengthens near the equator enough so that they are of a similar magnitude but opposite in sign. This implies that the thermodynamic SLHF may be considered an alternate mechanism for abating positive WES feedbacks. Thus, we investigate the anomalous $(Q_s - Q_a)$ terms to seek a deeper understanding of the structure of thermodynamic SLHF in Fig. 7.

For nITCZ events, there are large negative anomalies of $(Q_s - Q_a)$ from 5°S to 2°N that coincide with the latitudinal location of the anomalous cold tongue in SST (Fig. 4a) and a strong negative Q_s anomaly (Fig. 7c). This is unsurprising since surface saturation specific humidity is a function of surface temperature [Eq. (2)]. On the other hand, it is surprising that Q_a does not contain a strong dry anomaly near the equator (Fig. 7e). In fact, the Q_a anomalies have a better correspondence with lower boundary layer (1000–850 hPa) specific humidity anomalies (Fig. 7g). Thus, for nITCZ events, negative thermodynamic SLHF anomalies suppress positive dynamic SLHF anomalies because the cooler SSTs restrict the amount of moisture available for evaporation.

For dsITCZ events, there are strong negative $(Q_s - Q_a)$ anomalies south of 5°S and positive $(Q_s - Q_a)$ anomalies just south of the equator that are driven by significant anomalies in both Q_s and Q_a. Just like for nITCZ events, Q_s anomalies in Fig. 7d correspond well with SST anomalies in Fig. 4b for dsITCZ events. The strong negative $(Q_s - Q_a)$ south of 5°S can be explained by the aforementioned cold SST anomaly from 11° to 5°S in Fig. 4b as well as positive Q_a anomalies. Again, Q_a anomalies have a better correspondence with boundary layer specific humidity anomalies (Fig. 7h). Thus, negative thermodynamic SLHF anomalies constructively interfere with dynamic SLHF anomalies due to both cool SSTs and moist air above limiting evaporation. Just south of the equator, there is a weak positive (Q_s) anomaly (not statistically significant) and a strong negative (Q_a) anomaly collocated with the weak warm SST anomaly in Fig. 4b (not statistically significant). Therefore, for dsITCZ events, positive thermodynamic SLHF anomalies suppress negative dynamic SLHF anomalies just south of the equator because of drier air above the sea surface that decreases the amount of moisture available for evaporation.

Following Fig. 1a, the negative northward gradient of SLHF would work to increase SSTs to the north of the equator and decrease SSTs to the south of the equator, thus setting up the positive WES feedback mechanism. From our investigation of the fingerprints of the positive WES feedback mechanism, particularly Figs. 4c,d and 5c,d, we know that this positive WES feedback is not a runaway feedback and is abated by another process. Karnauskas (2022) suggests the simultaneous presence of a negative WES feedback mechanism that would work to curb the infinite increase of SST to the north and decrease to the south of the equator through vertical momentum mixing (Wallace et al. 1989; Hayes et al. 1989; Chelton et al. 2001). In the next subsection, we look at the structure of near-surface stability and the resulting dynamics and thermodynamics for the two types of ITCZ events.

Last, note that using Eq. (2), our observed SLHF anomalies (blue curves in Fig. 6) on their own amount to SST tendencies from about +0.25 to −0.25 K month^{-1} (Fig. S3). This is significant, especially when compared to the SST anomalies in Fig. 4.

c. *Negative WES feedback: Near-surface stability and vertical momentum mixing*

In this section, we assess both stability and vertical momentum mixing in the lower troposphere by analyzing near-surface temperature stratification and wind shear. This is guided by the fingerprints of the negative WES feedback mechanism discussed in section 2c.

Just like the positive WES mechanism discussed so far, a northward gradient of SST anomalies during nITCZ events (Fig. 4a) also sets the ground to initialize the WH89 negative WES feedback mechanism illustrated in Fig. 1b, column A. To move to column B in Fig. 1b, an alteration of the near-surface stability must be present. Figure 8a shows the distribution of zonally averaged (90°–125°W) anomalous SST minus 10-m air temperature at daily lags of 21 days before to 21 days after nITCZ and dsITCZ events.

During nITCZ events, SSTs are anomalously higher than 10-m air temperature from 2° to 10°N, with the maximum difference occurring at 5°–7°N that coincides with the ITCZ latitude (Fig. 2a). The anomalously colder temperature above and warmer temperature below create less stably stratified atmospheric conditions. South of 2°N all the way to almost 12°S, 10-m air temperatures are anomalously larger than SSTs, creating more stable near-surface conditions.

For dsITCZ events, SSTs are anomalously lower than 10-m air temperature in two regions: one south of the equator,

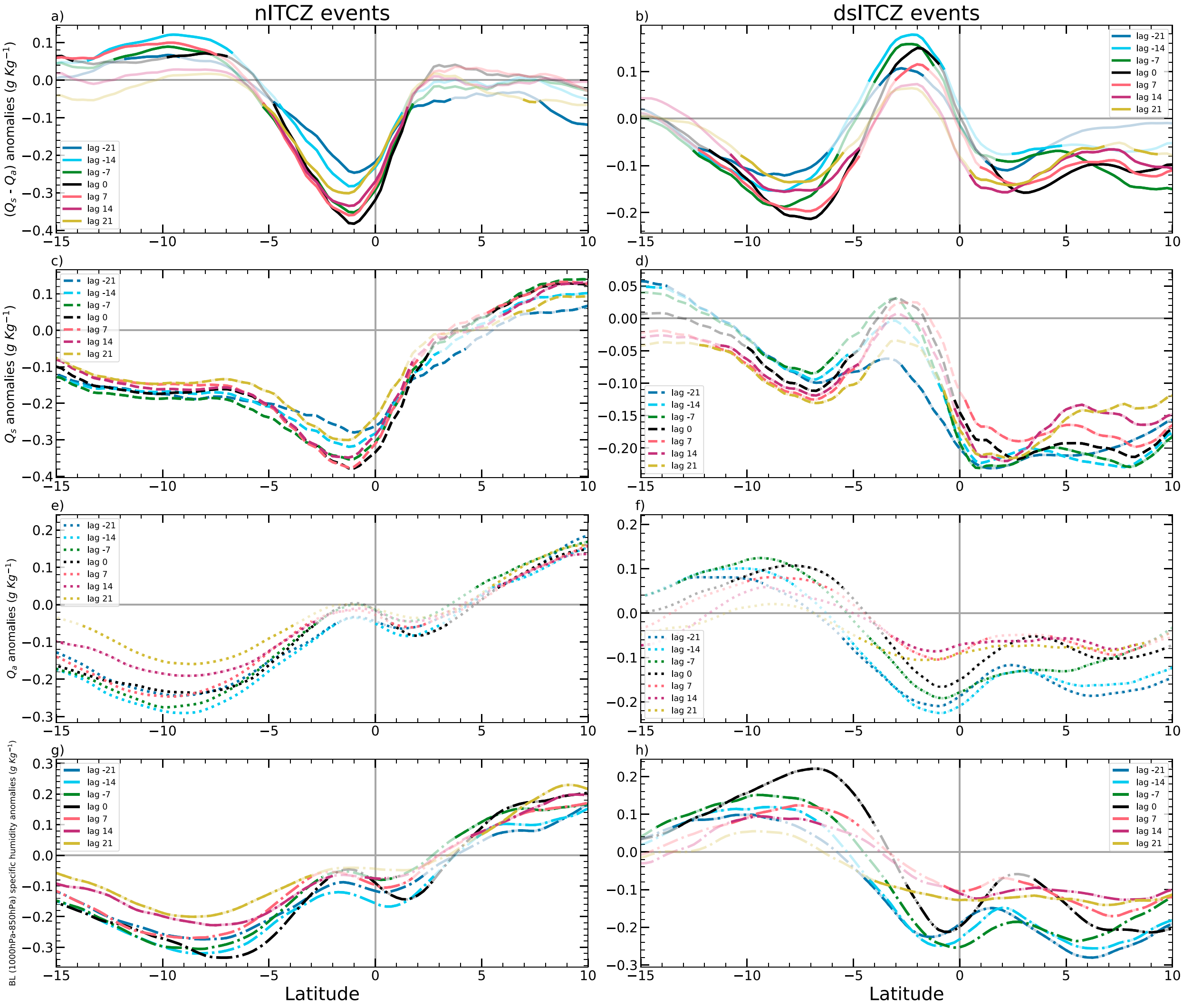

FIG. 7. (a),(b) The zonally averaged (90°–125°W) anomalous difference of surface saturation specific humidity Q_s and specific humidity of air Q_a for (left) nITCZ and (right) dsITCZ events. (c) Anomalous surface saturation specific humidity Q_s and (e) anomalous specific humidity of air Q_a for nITCZ events. (d),(f) As in (c) and (e), but for dsITCZ events. Anomalies of boundary layer (1000–850 hPa) specific humidity for (g) nITCZ and (h) dsITCZ events. Opaque lines show the fields at 95% confidence using a two-tailed t test.

from 8° to 15°S, and one north of 1°S (Fig. 2b). The anomalously colder temperatures below warmer temperatures in these regions indicate larger stability. From 1° to 9°S, the near-surface air is less stable than usual, with 10-m air temperatures being lesser than SST.

Since near-surface stability of the atmosphere is inversely related to the vertical momentum mixing according to the WH89 framework (illustrated by Fig. 1b, column C), we quantify the negative WES feedback mechanism by assessing how the vertical shear of zonal and meridional winds change for each ITCZ event relative to background climatology (shown in Fig. S4).

During nITCZ events (Fig. 8c), there are anomalously larger easterly winds at 100 m versus 10 m from 2° to 10°N that coincide with unstable near-surface conditions (Fig. 8a). Warmer SSTs in this region suggest more vertical mixing of zonal momentum. From 2°N to 10°S, 100-m zonal winds are weaker than winds at 10 m, corresponding to cooler SSTs and warmer 10-m air temperatures in that region. Cool surface below warm air suggests less vertical momentum mixing to the south of the equator.

For dsITCZ events (Fig. 8d), to the north of the equator and to the south of 7°S, there are stronger anomalous easterlies at 10 m than 100 m. This indicates less vertical mixing of zonal momentum, which corresponds well with negative values of (SST − T_{10}) and anomalously stable conditions. In the region from the equator to 7°S, there are anomalously weaker easterlies at 10 m below stronger easterlies at 100 m, which corresponds with more vertical mixing of zonal momentum due to unstable conditions (Fig. 8b).

During nITCZ events, the meridional 100-m minus 10-m winds are anomalously southerly from 10°N to 8°S and they

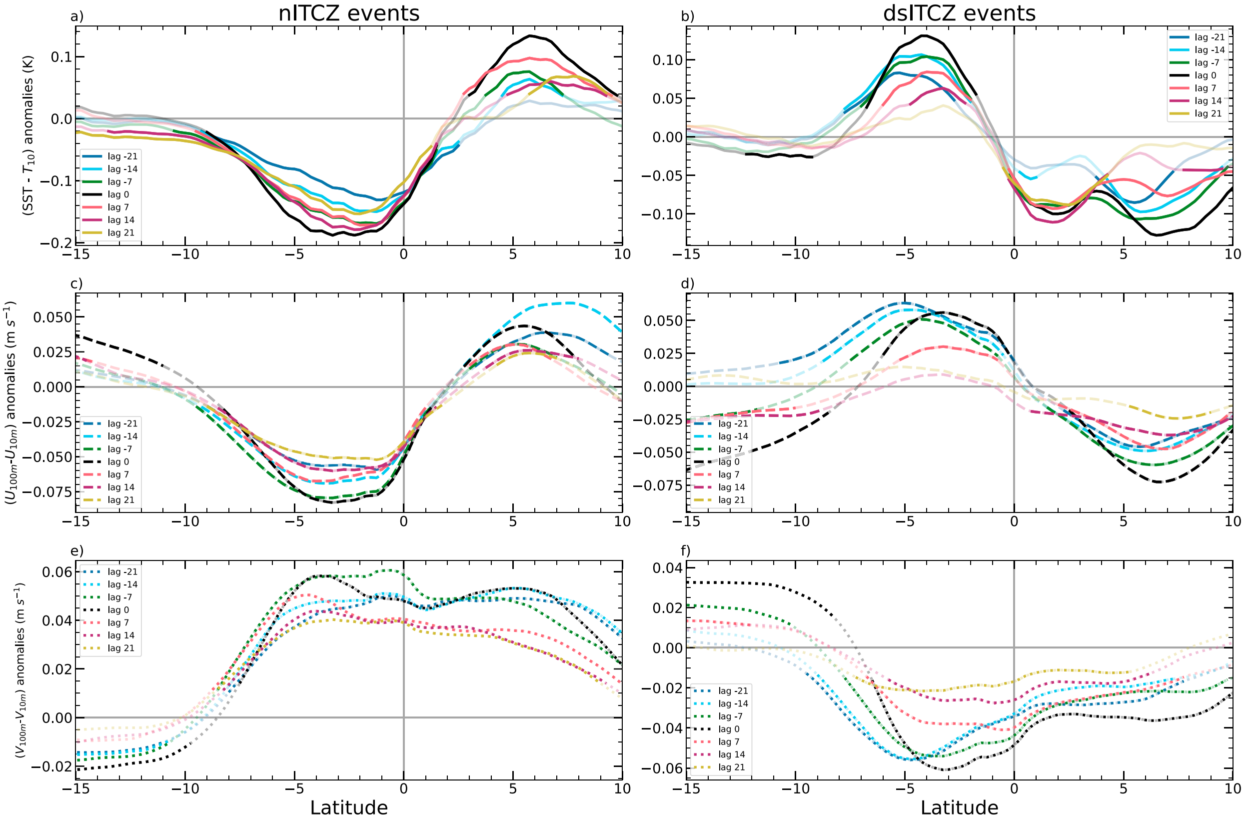

FIG. 8. Zonally averaged (90°–125°W) anomalous difference between (a),(b) SST and 10-m air temperature. (c),(d) 100- and 10-m zonal winds ($U_{100\mathrm{m}} - U_{10\mathrm{m}}$) and (e),(f) 100- and 10-m meridional winds ($V_{100\mathrm{m}} - V_{10\mathrm{m}}$) for (left) nITCZ and (right) dsITCZ events at 95% confidence, indicated in opaque lines.

become weak northerlies south of 8°S (Fig. 8e). Climatological meridional winds at 10 and 100 m are northerlies to the north of 4°N and southerlies to the south of 4°N (Fig. S4). From 4° to 10°N, therefore, anomalous southerlies over northerlies create weaker vertical wind shear and more vertical mixing.

For dsITCZ events (Fig. 8f), from 7° to 15°S, there are stronger 100-m meridional winds above weaker 10-m winds, creating anomalous southerlies, which indicates less vertical momentum mixing. Comparing to Fig. 8b, (SST − T_{10}) in this region is negative or close to zero, indicating stable near-surface temperature stratification. North of 4°N, anomalous northerlies on top of climatological northerlies create stronger wind shear and thus less momentum mixing in the vertical. Higher 10-m air temperature compared to SSTs in this region results in a more stable atmosphere.

This interpretation of anomalous winds is important because we cannot directly quantify column E of Fig. 1. Qualitatively, the anomalous easterlies resulting due to more momentum mixing in the warmer hemisphere act to amplify the background easterlies in this hemisphere, thus leading to an increase in the latent heat flux and vice versa for the cooler hemisphere (Fig. 1 column E). As a result, the anomalous SST gradient would become less pronounced. This chain of events establishes a negative feedback mechanism, with the warmer SSTs getting less warm and cooler SSTs becoming less cool.

d. *Time evolution of positive and negative WES feedback fingerprints*

Figure 9 shows the time evolution of the most critical fields that tie together the occurrence of the positive and negative WES mechanisms for nITCZ and dsITCZ events. Figures 9a and 9b show that SLHF gradients peak in strength at negative lags and they are nearly in phase with SST gradient tendencies for both nITCZ and dsITCZ events. This in-phase relationship between SLHF and SST tendencies corresponds well with Eq. (2), which is key to both negative and positive WES feedback mechanisms. The dynamic component of SLHF broadly describes this relationship between SLHF and SST tendencies, which signifies that at the very least positive WES feedbacks are occurring before these ITCZ events. However, note that the peak SLHF and SST gradients occur approximately 5–15 days earlier for dsITCZ events than nITCZ events. Figures 9c and 9d illustrate the importance of the thermodynamic SLHF component gradients in abating positive WES feedbacks through limiting evaporation near the equator. Note that the thermodynamic SLHF gradients are in phase with the SST gradients unlike the dynamic SLHF gradients, which are out of phase. In Figs. 9e and 9f, we can see

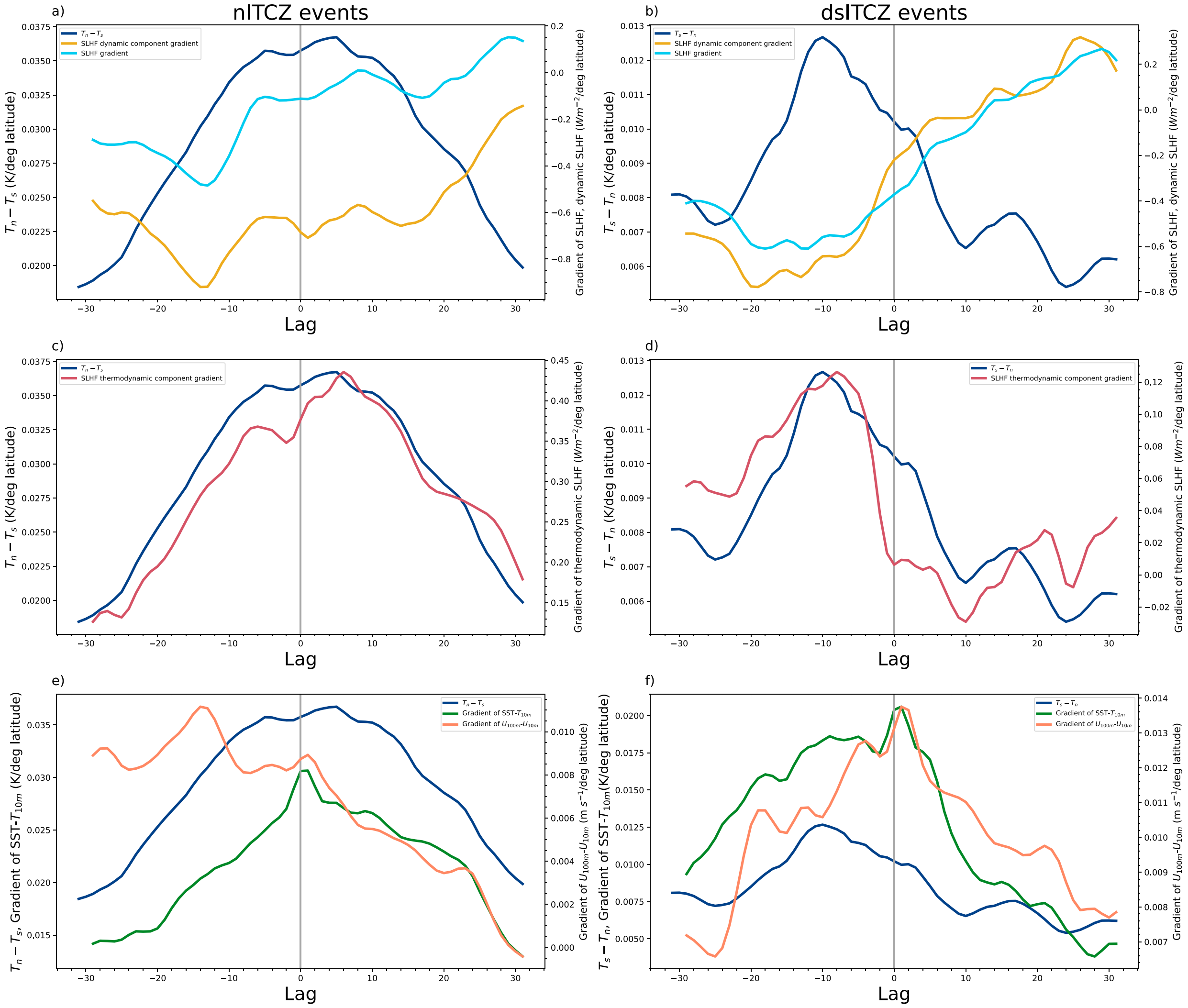

FIG. 9. Time evolution of (a),(b) cross-equatorial SST gradient, anomalous SLHF gradient, and gradient of dynamic component of SLHF; (c),(d) cross-equatorial SST gradient and gradient of thermodynamic component of SLHF; and (e),(f) cross-equatorial SST gradient, (SST − T_{10}) gradient, and zonal wind shear (100 m minus 10 m) gradient for (left) nITCZ and (right) dsITCZ events. All gradients are computed between the northern and southern latitudes highlighted in Figs. 4a and 4b.

the role of negative WES feedbacks through cross-equatorial gradients of SST minus 10-m air temperature (SST − T_{10}), which is a measure of vertical stratification, and 100-m minus 10-m zonal wind, which is a measure of zonal wind shear. For both nITCZ and dsITCZ events, the (SST − T_{10}) gradients peak strongly near lag 0 which implies a loose correlation with SST gradients for nITCZ events but a delayed response for dsITCZ events. Zonal wind shear gradients are generally in phase with (SST − T_{10}) gradients for dsITCZ events, which implies that about 10 days after the peak SST gradients, the negative WES feedback is strongest and likely contributes to the decrease in SST gradients. On the other hand, zonal wind shear gradients are not in phase with (SST − T_{10}) gradients for nITCZ events, peaking near lag −15, which complicates our interpretation of the role of negative WES feedbacks for nITCZ events.

4. Summary and conclusions

The latitudinal location of the ITCZ varies across a wide range of time scales, including seasonal as well as daily–weekly time scales over the east Pacific during February–April (Haffke et al. 2016; Gonzalez et al. 2022). In this study, we have investigated the latitudinal structure of near-surface dynamics and thermodynamics associated with submonthly Northern Hemisphere ITCZ (nITCZ) and double/Southern Hemisphere ITCZ (dsITCZ) events over the east Pacific through the lens of two opposing fingerprints of wind–evaporation–SST (WES) feedbacks in the ERA5 reanalysis. While earlier studies have shed light on the importance of the classical positive WES feedbacks on longer time scales (Lindzen and Nigam 1987; Xie and Philander 1994; Li and Xie 2014), analyzing the variability on time scales of days to weeks is relatively new. This study also focuses on the effect of

SST on near-surface vertical stratification and momentum mixing that results from negative WES feedbacks (Wallace et al. 1989; Hayes et al. 1989; Karnauskas 2022).

Based on our findings, the warmer SSTs to the north of the equator and colder to the south act as a seed for the classical WES feedback for a northern ITCZ to begin. The northward SST gradient results in a southward gradient of the MSLP, thus promoting the intensification of cross-equatorial southerly surface winds. Coriolis force results in the winds becoming anomalous westerlies (weak easterlies) to the north of the equator and stronger easterlies to the south of the equator. The gradient of SLHF, especially the dynamic SLHF component [Eq. (5)], is in phase with the SST tendency, that is, SSTs become warmer in the Northern Hemisphere and cool down further in the Southern Hemisphere prior to lag 0 of nITCZ events (Fig. 9a). Nearly the same structures (reversed direction) and order of processes exist for dsITCZ events with the exception that cross-equatorial SST gradients maximize 5–15 days earlier than nITCZ events.

We find that this basic dynamic component-dominant SLHF structure of positive WES feedbacks is altered for nITCZ and dsITCZ events near the equator mainly in the thermodynamic component of SLHF, that is, by a nonnegligible contribution of $\delta(Q_s - Q_a)$ [Eq. (5)]. We find that the thermodynamic component of SLHF acts against the positive WES feedback mechanism. We attribute the structure of $\delta(Q_s - Q_a)$ to differences between the anomalous SSTs (e.g., the anomalous cold tongue) and boundary layer humidity features (e.g., top of the boundary layer stability changes near 5°–10°S, not shown) that limit evaporation. Contrary to the dynamic component, the thermodynamic component of SLHF peaks in phase with SST rather than SST tendency.

The runaway positive WES feedback is controlled by the presence of a simultaneous negative WES feedback that starts off with similarly asymmetric SSTs about the equator but is driven by the vertical stratification of the atmosphere for both nITCZ and dsITCZ events. Relatively warmer SSTs near the ITCZ create warmer air at the surface below colder air at 10 m. Less stable air in the warmer hemisphere is associated with more mixing of vertical momentum, evident in smaller 100-m minus 10-m zonal wind shear. In the cooler hemisphere, cold surface below warmer 10-m air creates a stable environment, resulting in less vertical mixing of zonal momentum, seen through stronger 100-m minus 10-m zonal wind shear.

Because of climatological easterlies in the Northern Hemisphere and westerlies in the Southern Hemisphere, more mixing in the warmer hemisphere and less mixing in the cooler hemisphere lead to stronger surface easterlies and westerlies in the two hemispheres, respectively (Fig. 1b). The zonal and meridional wind shear (100–10 m) anomalies are structurally the same as the surface wind anomalies in Fig. 1a, meaning there is less evaporation (latent heat) in the cooler hemisphere and more in the warmer hemisphere. The net result is a weakening of the initial SST gradient, thus setting up a negative feedback mechanism.

We find that the negative WES feedback fingerprints (zonal wind shear and near-surface stratification) do indeed peak approximately 10 days after the peak cross-equatorial SST gradient for dsITCZ events. However, for nITCZ events, the gradient of vertical zonal wind shear is strongest about 2 weeks before the cross-equatorial SST gradients maximize, which is not entirely consistent with negative WES feedback theory. On the other hand, the near-surface temperature-stratification gradient is more consistent with the negative WES feedback theory, with a peak in strength near and after lag 0.

Therefore, this study shows the presence of both the mechanisms through composites of the dynamic and thermodynamic factors during the two most prevalent types of ITCZ events (nITCZ and dsITCZ). Both positive and negative feedback mechanisms are present and important during the evolution of the ITCZ on shorter time scales. Moreover, the spatial structure of the variables is almost mirror images for the opposing nITCZ and dsITCZ events. However, the timing is slightly different between dsITCZ and nITCZ events, with nITCZ events having a peak in cross-equatorial SST gradients near lag 0 and dsITCZ events having a cross-equatorial SST gradients maximizing near lag −10. We see a similar progression for both ITCZ events, with positive WES feedbacks occurring before the peak in cross-equatorial SST gradients, then the thermodynamic component of SLHF acting as a mitigating factor during the peak in cross-equatorial SST gradients, and finally the stratification aspects of negative WES feedbacks taking over after the peak in cross-equatorial SST gradients. This study provides a framework to build upon to effectively quantify the relative importance of the fingerprints of both positive and negative WES feedback mechanisms, as well as alternate mechanisms (e.g., the thermodynamic component of SLHF) in models and observations. It is especially important to apply our results to climate model representation of both WES feedback mechanisms over the east Pacific during February–April considering the fact that models produce more than normal precipitation to the south of the equator and less to the north of the equator during these months and over this region (Wang et al. 2015; Song and Zhang 2019; Baldwin et al. 2021; Si et al. 2021).

Moving forward, studying the ocean processes that control SST variability (e.g., temperature advection, Ekman pumping) and boundary layer temperature and humidity variations, possibly in relation to low clouds (Woelfle et al. 2019), would further build upon our understanding of air–sea–cloud coupling. This "double-ITCZ bias" that results is an overarching problem in climate models that affects more than the east Pacific (Adam et al. 2018), and considering the fact that the addition of an oceanic component to the models exacerbates the problem (Xiang et al. 2017), quantifying both WES feedback mechanisms through a similar analysis as this one is imperative.

Acknowledgments. The authors thank Dr. Spencer Hill for fruitful discussions that helped us in developing ideas for this manuscript. Financial support comes from NSF Grant AGS-1953944 and startup funding from Iowa State University.

Data availability statement. The TMPA data can be downloaded from https://disc.gsfc.nasa.gov/datasets/TRMM_3B42_Daily_7/summary. The ERA5 reanalysis surface data can be downloaded from https://cds.climate.copernicus.eu/cdsapp#!/dataset/reanalysis-era5-single-levels?tab=overview. All scripts used to produce figures for this paper are located online via the repository https://drive.google.com/drive/folders/19HvXbsOL1Ui-jzcbd4QD4MOhT1S_F-ju?usp=sharing.

REFERENCES

Adam, O., T. Bischoff, and T. Schneider, 2016a: Seasonal and interannual variations of the energy flux equator and ITCZ. Part I: Zonally averaged ITCZ position. *J. Climate*, **29**, 3219–3230, https://doi.org/10.1175/JCLI-D-15-0512.1.

——, ——, and ——, 2016b: Seasonal and interannual variations of the energy flux equator and ITCZ. Part II: Zonally varying shifts of the ITCZ. *J. Climate*, **29**, 7281–7293, https://doi.org/10.1175/JCLI-D-15-0710.1.

——, T. Schneider, and F. Brient, 2018: Regional and seasonal variations of the double-ITCZ bias in CMIP5 models. *Climate Dyn.*, **51**, 101–117, https://doi.org/10.1007/s00382-017-3909-1.

Baldwin, J. W., A. R. Atwood, G. A. Vecchi, and D. S. Battisti, 2021: Outsize influence of Central American orography on global climate. *AGU Adv.*, **2**, e2020AV000343, https://doi.org/10.1029/2020AV000343.

Bellucci, A., S. Gualdi, and A. Navarra, 2010: The double-ITCZ syndrome in coupled general circulation models: The role of large-scale vertical circulation regimes. *J. Climate*, **23**, 1127–1145, https://doi.org/10.1175/2009JCLI3002.1.

Bischoff, T., and T. Schneider, 2014: Energetic constraints on the position of the intertropical convergence zone. *J. Climate*, **27**, 4937–4951, https://doi.org/10.1175/JCLI-D-13-00650.1.

——, and ——, 2016: The equatorial energy balance, ITCZ position, and double-ITCZ bifurcations. *J. Climate*, **29**, 2997–3013, https://doi.org/10.1175/JCLI-D-15-0328.1.

Bjerknes, J., L. J. Allison, E. R. Kreins, F. A. Godshall, and G. Warnecke, 1969: Satellite mapping of the Pacific tropical cloudiness. *Bull. Amer. Meteor. Soc.*, **50**, 313–322, https://doi.org/10.1175/1520-0477-50.5.313.

Broccoli, A. J., K. A. Dahl, and R. J. Stouffer, 2006: Response of the ITCZ to Northern Hemisphere cooling. *Geophys. Res. Lett.*, **33**, l01702, https://doi.org/10.1029/2005GL024546.

Chelton, D. B., and Coauthors, 2001: Observations of coupling between surface wind stress and sea surface temperature in the eastern tropical Pacific. *J. Climate*, **14**, 1479–1498, https://doi.org/10.1175/1520-0442(2001)014<1479:OOCBSW>2.0.CO;2.

Chiang, J. C. H., and C. M. Bitz, 2005: Influence of high latitude ice cover on the marine intertropical convergence zone. *Climate Dyn.*, **25**, 477–496, https://doi.org/10.1007/s00382-005-0040-5.

——, and A. R. Friedman, 2012: Extratropical cooling, interhemispheric thermal gradients, and tropical climate change. *Annu. Rev. Earth Planet. Sci.*, **40**, 383–412, https://doi.org/10.1146/annurev-earth-042711-105545.

Colose, C. M., A. N. LeGrande, and M. Vuille, 2016: Hemispherically asymmetric volcanic forcing of tropical hydroclimate during the last millennium. *Earth Syst. Dyn.*, **7**, 681–696, https://doi.org/10.5194/esd-7-681-2016.

ECMWF, 2016: Part IV: Physical processes. IFS Doc. CY41R2, ECMWF, 213 pp., https://www.ecmwf.int/sites/default/files/elibrary/2016/79697-ifs-documentation-cy41r2-part-iv-physical-processes_1.pdf.

Fairall, C. W., E. F. Bradley, J. E. Hare, A. A. Grachev, and J. B. Edson, 2003: Bulk parameterization of air–sea fluxes: Updates and verification for the COARE algorithm. *J. Climate*, **16**, 571–591, https://doi.org/10.1175/1520-0442(2003)016<0571:BPOASF>2.0.CO;2.

Fiedler, S., and Coauthors, 2020: Simulated tropical precipitation assessed across three major phases of the Coupled Model Intercomparison Project (CMIP). *Mon. Wea. Rev.*, **148**, 3653–3680, https://doi.org/10.1175/MWR-D-19-0404.1.

Frierson, D. M. W., and Y.-T. Hwang, 2012: Extratropical influence on ITCZ shifts in slab ocean simulations of global warming. *J. Climate*, **25**, 720–733, https://doi.org/10.1175/JCLI-D-11-00116.1.

Gonzalez, A. O., I. Ganguly, M. C. McGraw, and J. G. Larson, 2022: Rapid dynamical evolution of ITCZ events over the east Pacific. *J. Climate*, **35**, 1197–1213, https://doi.org/10.1175/JCLI-D-21-0216.1.

Haffke, C., G. Magnusdottir, D. Henke, P. Smyth, and Y. Peings, 2016: Daily states of the March–April east Pacific ITCZ in three decades of high-resolution satellite data. *J. Climate*, **29**, 2981–2995, https://doi.org/10.1175/JCLI-D-15-0224.1.

Hayes, S. P., M. J. McPhaden, and J. M. Wallace, 1989: The influence of sea surface temperature on surface wind in the eastern equatorial Pacific: Weekly to monthly variability. *J. Climate*, **2**, 1500–1506, https://doi.org/10.1175/1520-0442(1989)002<1500:TIOSST>2.0.CO;2.

Henke, D., P. Smyth, C. Haffke, and G. Magnusdottir, 2012: Automated analysis of the temporal behavior of the double intertropical convergence zone over the east Pacific. *Remote Sens. Environ.*, **123**, 418–433, https://doi.org/10.1016/jrse.2012.03.022.

Hersbach, H., and Coauthors, 2020: The ERA5 global reanalysis. *Quart. J. Roy. Meteor. Soc.*, **146**, 1999–2049, https://doi.org/10.1002/qj.3803.

Huffman, G. J., and D. T. Bolvin, 2015: TRMM and other data precipitation data set documentation. NASA TRMM Doc., 44 pp., https://pmm.nasa.gov/sites/default/files/document_files/3B42_3B43_doc_V7.pdf.

Hwang, Y.-T., and D. M. W. Frierson, 2013: Link between the double-intertropical convergence zone problem and cloud biases over the Southern Ocean. *Proc. Natl. Acad. Sci. USA*, **110**, 4935–4940, https://doi.org/10.1073/pnas.1213302110.

Jean-Michel, L., and Coauthors, 2021: The Copernicus global 1/12° oceanic and sea ice glorys12 reanalysis. *Front. Earth Sci.*, **9**, 698876, https://doi.org/10.3389/feart.2021.698876.

Kang, S. M., I. M. Held, D. M. W. Frierson, and M. Zhao, 2008: The response of the ITCZ to extratropical thermal forcing: Idealized slab-ocean experiments with a GCM. *J. Climate*, **21**, 3521–3532, https://doi.org/10.1175/2007JCLI2146.1.

Karnauskas, K. B., 2022: A simple coupled model of the wind–evaporation–SST feedback with a role for stability. *J. Climate*, **35**, 2149–2160, https://doi.org/10.1175/JCLI-D-20-0895.1.

Knapp, K. R., and Coauthors, 2011: Globally gridded satellite observations for climate studies. *Bull. Amer. Meteor. Soc.*, **92**, 893–907, https://doi.org/10.1175/2011BAMS3039.1.

Lellouche, J.-M., and Coauthors, 2018: Recent updates to the Copernicus marine service global ocean monitoring and forecasting real-time 1/12° high-resolution system. *Ocean Sci.*, **14**, 1093–1126, https://doi.org/10.5194/os-14-1093-2018.

Li, G., and S.-P. Xie, 2014: Tropical biases in CMIP5 multimodel ensemble: The excessive equatorial Pacific cold tongue and double ITCZ problems. *J. Climate*, **27**, 1765–1780, https://doi.org/10.1175/JCLI-D-13-00337.1.

Li, T., and S. G. H. Philander, 1996: On the annual cycle of the eastern equatorial Pacific. *J. Climate*, **9**, 2986–2998, https://doi.org/10.1175/1520-0442(1996)009<2986:OTACOT>2.0.CO;2.

Lin, J.-L., 2007: The double-ITCZ problem in IPCC AR4 coupled GCMs: Ocean–atmosphere feedback analysis. *J. Climate*, **20**, 4497–4525, https://doi.org/10.1175/JCLI4272.1.

Lindzen, R. S., and S. Nigam, 1987: On the role of sea surface temperature gradients in forcing low-level winds and convergence in the tropics. *J. Atmos. Sci.*, **44**, 2418–2436, https://doi.org/10.1175/1520-0469(1987)044<2418:OTROSS>2.0.CO;2.

Mechoso, C. R., and Coauthors, 1995: The seasonal cycle over the tropical Pacific in coupled ocean-atmosphere general circulation models. *Mon. Wea. Rev.*, **123**, 2825–2838, https://doi.org/10.1175/1520-0493(1995)123<2825:TSCOTT>2.0.CO;2.

Oueslati, B., and G. Bellon, 2015: The double ITCZ bias in CMIP5 models: Interaction between SST, large-scale circulation and precipitation. *Climate Dyn.*, **44**, 585–607, https://doi.org/10.1007/s00382-015-2468-6.

Pausata, F. S. R., L. Chafik, R. Caballero, and D. S. Battisti, 2015: Impacts of high-latitude volcanic eruptions on ENSO and AMOC. *Proc. Natl. Acad. Sci. USA*, **112**, 13 784–13 788, https://doi.org/10.1073/pnas.1509153112.

Philander, S. G. H., D. Gu, G. Lambert, T. Li, D. Halpern, N.-C. Lau, and R. C. Pacanowski, 1996: Why the ITCZ is mostly north of the equator. *J. Climate*, **9**, 2958–2972, https://doi.org/10.1175/1520-0442(1996)009<2958:WTIIMN>2.0.CO;2.

Schneider, T., 2017: Feedback of atmosphere-ocean coupling on shifts of the intertropical convergence zone. *Geophys. Res. Lett.*, **44**, 11 644–11 653, https://doi.org/10.1002/2017GL075817.

Si, W., H. Liu, X. Zhang, and M. Zhang, 2021: Double intertropical convergence zones in coupled ocean-atmosphere models: Progress in CMIP6. *Geophys. Res. Lett.*, **48**, e2021GL094779, https://doi.org/10.1029/2021GL094779.

Siler, N., G. H. Roe, K. C. Armour, and N. Feldl, 2019: Revisiting the surface-energy-flux perspective on the sensitivity of global precipitation to climate change. *Climate Dyn.*, **52**, 3983–3995, https://doi.org/10.1007/s00382-018-4359-0.

Song, X., and G. J. Zhang, 2019: Culprit of the eastern Pacific double-ITCZ bias in the NCAR CESM1.2. *J. Climate*, **32**, 6349–6364, https://doi.org/10.1175/JCLI-D-18-0580.1.

Tetens, O., 1930: Uber einige meteorologische begriffe. *Z. Geophys.*, **6**, 297–309.

Tian, B., and X. Dong, 2020: The double-ITCZ bias in CMIP3, CMIP5, and CMIP6 models based on annual mean precipitation. *Geophys. Res. Lett.*, **47**, e2020GL087232, https://doi.org/10.1029/2020GL087232.

Voigt, A., S. Bony, J.-L. Dufresne, and B. Stevens, 2014: The radiative impact of clouds on the shift of the intertropical convergence zone. *Geophys. Res. Lett.*, **41**, 4308–4315, https://doi.org/10.1002/2014GL060354.

Waliser, D. E., and C. Gautier, 1993: A satellite-derived climatology of the ITCZ. *J. Climate*, **6**, 2162–2174, https://doi.org/10.1175/1520-0442(1993)006<2162:ASDCOT>2.0.CO;2.

Wallace, J. M., T. P. Mitchell, and C. Deser, 1989: The influence of sea-surface temperature on surface wind in the eastern equatorial Pacific: Seasonal and interannual variability. *J. Climate*, **2**, 1492–1499, https://doi.org/10.1175/1520-0442(1989)002<1492:TIOSST>2.0.CO;2.

Wang, C.-C., W.-L. Lee, Y.-L. Chen, and H.-H. Hsu, 2015: Processes leading to double intertropical convergence zone bias in CESM1/CAM5. *J. Climate*, **28**, 2900–2915, https://doi.org/10.1175/JCLI-D-14-00622.1.

Woelfle, M. D., C. S. Bretherton, C. Hannay, and R. Neale, 2019: Evolution of the double-ITCZ bias through CESM2 development. *J. Adv. Model. Earth Syst.*, **11**, 1873–1893, https://doi.org/10.1029/2019MS001647.

Xiang, B., M. Zhao, I. M. Held, and J.-C. Golaz, 2017: Predicting the severity of spurious "double ITCZ" problem in CMIP5 coupled models from AMIP simulations. *Geophys. Res. Lett.*, **44**, 1520–1527, https://doi.org/10.1002/2016GL071992.

——, ——, Y. Ming, W. Yu, and S. M. Kang, 2018: Contrasting impacts of radiative forcing in the Southern Ocean versus southern tropics on ITCZ position and energy transport in one GFDL climate model. *J. Climate*, **31**, 5609–5628, https://doi.org/10.1175/JCLI-D-17-0566.1.

Xie, S.-P., and S. G. H. Philander, 1994: A coupled ocean-atmosphere model of relevance to the ITCZ in the eastern Pacific. *Tellus*, **46A**, 340–350, https://doi.org/10.3402/tellusa.v46i4.15484.

Yang, W., and G. Magnusdottir, 2016: Interannual signature in daily ITCZ states in the east Pacific in boreal spring. *J. Climate*, **29**, 8013–8025, https://doi.org/10.1175/JCLI-D-16-0395.1.

——, G. A. Vecchi, S. Fueglistaler, L. W. Horowitz, D. J. Luet, A. G. Muñoz, D. Paynter, and S. Underwood, 2019: Climate impacts from large volcanic eruptions in a high-resolution climate model: The importance of forcing structure. *Geophys. Res. Lett.*, **46**, 7690–7699, https://doi.org/10.1029/2019GL082367.

Zhang, C., 2001: Double ITCZs. *J. Geophys. Res.*, **106**, 11 785–11 792, https://doi.org/10.1029/2001JD900046.

Zhang, G. J., X. Song, and Y. Wang, 2019: The double ITCZ syndrome in GCMS: A coupled feedback problem among convection, clouds, atmospheric and ocean circulations. *Atmos. Res.*, **229**, 255–268, https://doi.org/10.1016/j.atmosres.2019.06.023.

Zhang, X., L. Hailong, and Z. Minghua, 2015: Double ITCZ in coupled ocean-atmosphere models: From CMIP3 to CMIP5. *Geophys. Res. Lett.*, **42**, 8651–8659, https://doi.org/10.1002/2015GL065973.